GEOPHYSICAL RESEARCH LETTERS, VOL. 37, L08107, doi:10.1029/2010GL042964, 2010

Energetic, ~5–90 keV neutral atom imaging of a weak substorm with STEREO/STE

Linghua Wang,[1] R. P. Lin,[1,2,3] G. K. Parks,[1] P. C. Brandt,[4] E. C. Roelof,[4] J. G. Sample,[1] J. P. Eastwood,[1,5] D. E. Larson,[1] D. W. Curtis,[1] and J. G. Luhmann[1]

Received 18 February 2010; accepted 22 March 2010; published 30 April 2010.

[1] We present imaging and high resolution energy spectra of energetic ~5–90 keV neutral atoms (ENA) of a weak geomagnetic substorm (Dst > −8 nT and AE ≲ 200 nT), made by the Suprathermal Electron (STE) instrument on the STEREO B spacecraft. Enhanced ENA emissions were observed coming from around local midnight near the equator with different spatial distribution and/or temporal behavior at ~5–20keV compared to ~20–90 keV. By forward modeling using a parameterized ring-current model, we show that the ENA images imply the parent equatorial protons have pitch-angle distributions peaked at 90°, an energy spectrum consistent with *in situ* proton measurements at geosynchronous orbit, and a spatial asymmetry with the maximum flux at midnight for 5–20 keV and at 2240 MLT for 20–90 keV. These are the first ENA measurements at ~5 to 26 keV from low altitude, and the first for such weak activity. **Citation:** Wang, L., R. P. Lin, G. K. Parks, P. C. Brandt, E. C. Roelof, J. G. Sample, J. P. Eastwood, D. E. Larson, D. W. Curtis, and J. G. Luhmann (2010), Energetic, ~5–90 keV neutral atom imaging of a weak substorm with STEREO/STE, *Geophys. Res. Lett.*, *37*, L08107, doi:10.1029/2010GL042964.

1. Introduction

[2] Energetic ions in the Earth's magnetosphere can charge exchange with cold geocoronal neutrals to produce energetic neutral atoms (ENAs) that retain the parent ion's velocity and freely escape along a straight line (since the gravitational potential energy is <0.7 eV/nucleon). Remote ENA imaging of magnetospheric energetic ions was first demonstrated with IMP 7 & 8 and ISEE 1 observations of 50 keV ENAs [*Roelof et al.*, 1985; *Roelof*, 1987]. Since then, ENAs have been used to remotely image the ring current during geomagnetic storms and substorms [e.g., *Henderson et al.*, 1997; *Pollock et al.*, 2003; *Vallat et al.*, 2004], mostly from spacecraft at high altitudes, outside the trapped radiation belts. IMAGE extended the energies down to ~1 keV [e.g., *Mitchell et al.*, 2001; *Pollock et al.*, 2001], and Astrid-1 made ~26–37 keV ENA measurements in the polar cap and near the equator from low Earth orbit (LEO, ~1000 km) [*C:son Brandt et al.*, 2001, 2002b]. These ENA images revealed brighter ENA emissions from the ring current on the night side during strong (Dst ≲ −50 nT) and moderate (Dst ~ −20 nT) geomagnetic activity. Forward modeling of the images [e.g., *C:son Brandt et al.*, 2002a] showed that the ring-current ions had a strong day/night flux asymmetry with the maximum on the night side, as expected from plasma injections during geomagnetic storms and substorms [*Roelof*, 1987; *Henderson et al.*, 1997].

[3] Here we present high sensitivity observations made by the STE (SupraThermal Electron) instrument on the STEREO B spacecraft at low altitude on the Earth's night side, showing enhanced 5–90 keV ENA emissions from the midnight region associated with the decay of a very weak substorm. The ENA emissions at 5–20 keV and at 20–90 keV differ in temporal variation and/or in source size and location.

2. Observations

[4] During the first three months after launch (October 2006), the two 3-axis-stabilized STEREO spacecraft were in elliptical orbits going from near Earth to beyond the moon. The STE instrument [*Lin et al.*, 2008] of the IMPACT investigation [*Luhmann et al.*, 2008] for STEREO utilizes arrays of small, passively cooled, thin window silicon semiconductor detectors (SSDs), coupled to state-of-the-art pulse-reset front-end electronics, to detect electrons down to ~2 keV (versus typical SSD thresholds of ~20–30 keV) and provide much greater sensitivity than the electrostatic analyzers used previously. STE also detects ions, neutrals, and X-rays [see *Hsieh et al.*, 2009] that penetrate the window and deposit ≳2 keV in the SSD active volume. EUV/UV/visible light is absorbed in the SSD window leading to increased leakage current, but at the level of geocoronal emissions the STE performance is unaffected. STE also provides intrinsic energy resolution of ≲1 keV FWHM (full width at half maximum), with the particles counts binned into energy channels of width ~0.5 keV up to ~10 keV, slowly increasing to ΔE/E ~ 20% above ~50 keV. Two oppositely directed sets of four detectors - STE-U(0, 1, 2, 3) and STE-D(0, 1, 2, 3) observe particles coming from and toward the Sun, with field of view (FOV) of 57° × 14.5° and 65° × 16.8° FWHM, forming a total FOV of 57° × 58° and 65° × 67° FWHM, respectively.

[5] On 6 November 2006 during a perigee pass, STE made observations from 0742 to 0749UT when STEREO B was traveling from 18.9° N geomagnetic latitude to 5.9° N at altitude of 510–840 km (L < 1.15) on the Earth's night

[1]Space Sciences Laboratory, University of California, Berkeley, California, USA.
[2]Physics Department, University of California, Berkeley, California, USA.
[3]School of Space Research, Kyung Hee University, Yongin, Korea.
[4]Johns Hopkins University Applied Physics Laboratory, Laurel, Maryland, USA.
[5]Blackett Laboratory, Imperial College London, London, UK.

0094-8276/10/2010GL042964

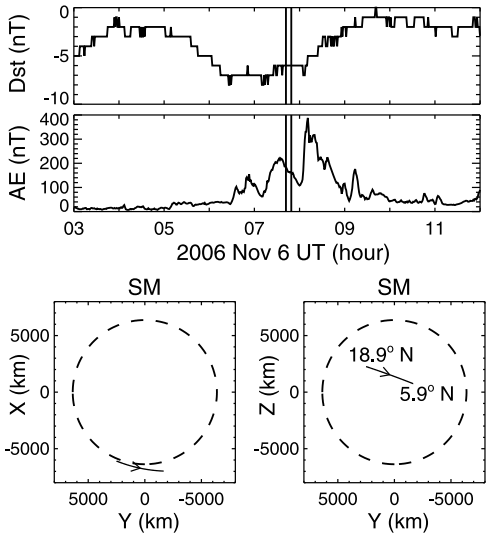

Figure 1. The (top) 1-minute DST index and (middle) AE index recorded between 03–12UT on 6 November 2006. The vertical lines indicate the STE observation interval between 0742–0749UT. The trajectory of STEREO B during 0742–0749UT, projected onto the X-Y plane (bottom left) and Z-Y plane (bottom right) of the SM coordinate, with arrow indicating the direction of motion. The dash-line circle represents the Earth's outline.

side (Figure 1 (bottom)). Thus, sunlight and auroral X-rays were blocked, while contamination from the X-ray flux of galactic sources was negligible. STE-D observed particles coming toward the Earth while STE-U observed particles coming from below. On this day, the Dst index (Figure 1 (top)) was $\gtrsim -8$ nT, but the Auroral Electroject (AE) index showed a series of small substorms (Figure 1 (middle)); the STE observations (vertical lines) were during the recovery phase of a small substorm (AE ~ 200 nT).

[6] Figure 2 shows examples of 30-second averaged observations and simulations at ~0745UT at 6.4 keV (left) and 34.2 keV (right), displayed in the Hammer-Aitoff map projection [*Snyder*, 1987] of the entire sky (north at top and south at bottom) viewed from the spacecraft, with the limb of the Earth (red curve) and the L = 4 and L = 8 dipole field lines (black solid curves) at dawn, midnight and dusk (the Earth blocks noon field lines) indicated. The blue lines indicate the iso-pitch-angle contours (30°, 60°, 90°, 120° and 150° pitch angle) of the local magnetic field at the spacecraft position. The FWHM FOVs of the four STE-U (looking earthward) and four STE-D (looking tailward) detectors are color-coded with their particle fluxes, from maximum (red) to minimum (indigo) for images observed at 6.4 keV (Figures 2a-b) and 34.2 keV (2e-f). The observed fluxes of particles coming toward Earth (STE-D) are ~4 times stronger at 6.4 keV and ~10 times stronger at 34.2 keV, than fluxes of particles going away (STE-U). STEREO B was doing a roll maneuver, so the FOV of STE-D scanned the nightside magnetosphere from extremes of ~50°N and ~90°W (dusk) to ~60°S and ~70°E (dawn) during 0742–0749UT. Averaged over the four SSDs of STE-D, the flux at 6.4 keV (representative of the ~5–20 keV range) stays constant within ~20% with time (Figure 2d), while the flux at 34.2 keV (representative of 20–70 keV) decreases with time by about a factor of 2 (Figure 2h).

[7] We believe that STE-U observed charged particles trapped on low-lying field lines (L < 1.15), because its fluxes fit a PAD increasing towards 90° (Figure 3 (top)), consistent with the pancake PADs of trapped particles [*Moritz*, 1972; *Guzik et al.*, 1989]. Trapped charged particle PADs, however, would be symmetric about 90°, while the fluxes measured by the upward looking STE-D were much higher than the STE-U charged particle fluxes (Figure 3 (top)), indicating they were dominated by fluxes of ENAs from the ring current on the night side. The squares in bottom of Figure 3 show a high energy resolution spectrum of ~5–90 keV ENAs measured at ~0745UT by detector STE-D3 that corresponds to the maximum flux (red regions in Figures 2a–2b and 2e–2f), showing a double power-law spectrum with a steepening above ~20 keV. The triangles show that the fluxes observed by STE-U2, representing the typical charged particle measurements in STE-U, are ~4–30 times smaller than the STE-D3 fluxes. The ENA fluxes in STE-D (squares in Figure 3) were estimated by subtracting the STE-U charged particle contribution. Because at all energies during 0742–0749UT, the probable contribution from locally trapped charged particles was generally ~5–30% of ENA intensities, we neglect the charged particle contribution in our analysis below.

3. Extraction of Parent Proton Distribution and Energy Spectrum

[8] Here we use the multi-parameter forward model for the equatorial ring current proton distribution developed for analysis of the IMAGE/HENA ENA images [*Roelof and Skinner*, 2000; *C:son Brandt et al.*, 2001], consisting of the MLT (magnetic local time) dependence of $e^{-k\times[1-\cos(\phi-\phi_0)]}$, the L dependence involving piece-wise exponentials and Gaussians in L, and the PAD of $(1 + m \times \sin^n \alpha)/(1 + m)$, where ϕ is the azimuthal angle and α is the pitch angle. First, the ENA flux, j_{ENA}, is calculated from the line-of-sight integral:

$$j_{ENA} = \int_0^\infty \sigma j_P(l) n_H(l) dl, \quad (1)$$

where l is the distance from the spacecraft, n_H is the number density of geocoronal hydrogen [*Østgaard et al.*, 2003], and σ is the charge exchange cross section between proton and neutral hydrogen. The proton flux j_P is defined by the parameterized ring-current model cited above. ENA stripping by hydrogen and oxygen as well as inelastic scattering has been neglected since these processes are insignificant at altitudes above 500 km [*DeMajistre et al.*, 2008]. Second, the ENA image is simulated by binning the neutral fluxes calculated along each line of sight for the angular response of each STE-D detector. Finally, we adjust the parameters of ring-current model and compare the simulated ENA image with the observed image, until a match is achieved.

[9] We make the simplifying assumptions that the ENA emission does not evolve during the 7-minute observation time, and that the parent proton distributions from 5 to

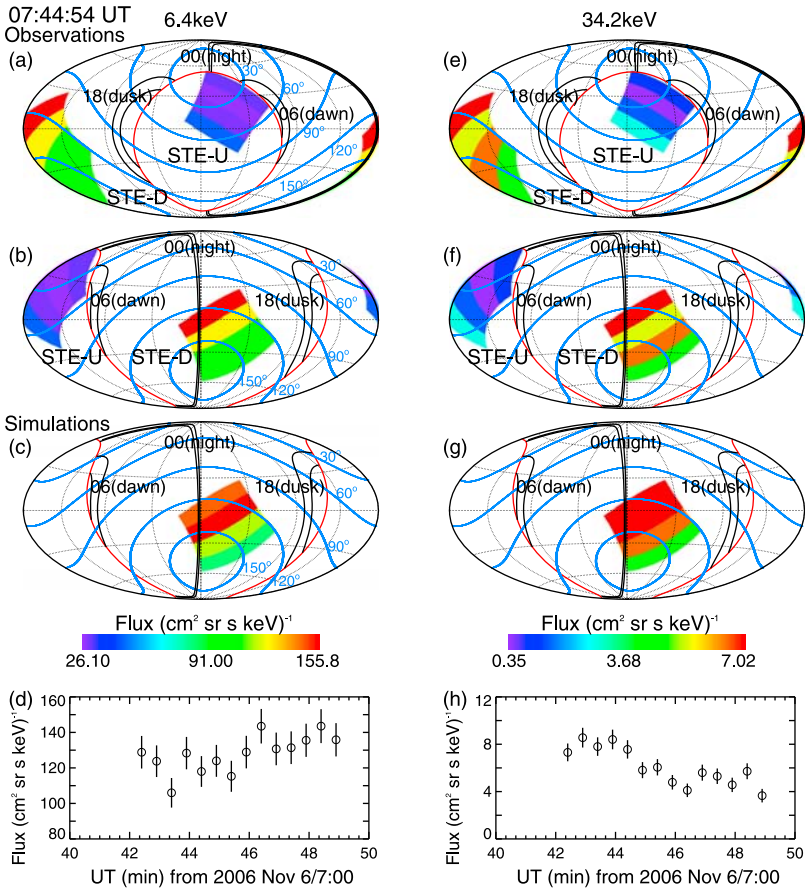

Figure 2. Examples of observed 30-second exposure ENA image and simulated image at (a–c) 6.4 keV and (e–g) 34.2 keV at 0745UT on 6 November 2006 (see text for details). Figures 2a and 2e and Figures 2b and 2f show the observed ENA image with the center being the earthward direction and the tailward direction, respectively. Figures 2c and 2g show the simulated image that is color-coded using the same color scale as the observed images. Figures 2d and 2h show the averaged flux in STE-D (looking tailward) versus time at 6.4 and 34.2 keV, respectively. The error bar is determined by the square root of the accumulated count.

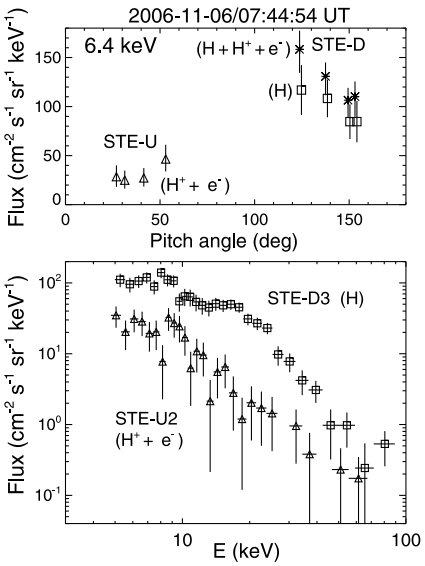

Figure 3. (top) The observed flux versus pitch angle for 6.4 keV at 0745 UT on 06 November 2006. The pitch angle is calculated for the center of FOV for each detector. The triangles represent the charged particle fluxes from STE-U, while the asterisks show the total (charged and neutral) fluxes from STE-D. The squares are the estimated ENA fluxes in STE-D after subtracting the charged particle contribution. (bottom) The energy spectra of ENA fluxes and locally trapped charged particle fluxes at 0745 UT. The squares indicate the ENA flux observed by detector STE-D3, after subtracting the charged particle contribution. The triangles show the flux of locally trapped protons and electrons detected by STE-U2. The error bar on the flux is determined by the square root of the accumulated count, and the error bar on the energy indicates the energy band for each energy channel.

20 keV have the same MLT dependence and PAD, and similarly from 20 to 90 keV. Then the match is obtained by minimizing a chi-square function - the sum of the squared difference between observed and simulated pixel counts, each divided by the observed count, over all energies below (above) 20 keV and times during 0742–0749UT. Our forward modeling shows that the morphology of the ENA images is sensitive to the shape of MLT distribution and PAD (isotropic, "pancake" or bi-directional) of equatorial protons, but is insensitive to the L-shell distribution (because the lines of sight almost always penetrate the whole range of L, we were unable to resolve the L-dependence). We therefore used an L-distribution that has a normalized proton intensity varying by only ~10% from the peak at L = 4 to L = 8, with steep decreases to near zero at L = 3 and L = 10.

[10] Figures 2c and 2g show the best-fit simulated ENA images for 6.4 and 34.2 keV from comparison to the observations at 0745 UT. For ~5–20 keV energies, the modeled proton PAD (Figure 4a) has a maximum at 90° (pancake), consistent with typical in situ proton observations during the late phase of geomagnetic storms [*Frank*, 1967; *Chen et al.*, 1998]. The spatial distribution of the modeled equatorial proton fluxes at 90° pitch angle, displayed in L (radial) versus MLT (azimuthal) coordinates, shows a spatial asymmetry with the maximum flux at midnight (Figure 4b) and a FWHM of 145°; however, a symmetric distribution (constant with MLT) is only a slightly worse fit (16% increase in chi-squar). For ~20–90 keV energies, the modeled proton PAD (Figure 4d) is also pancake-shaped, but the spatial distribution of the modeled equatorial proton fluxes peaks at 2240 MLT (pre-midnight) with a FWHM of 80°. In both energy ranges (Figures 4c and 4f), the modeled proton fluxes at 90° pitch angle (open circles) for 2043 MLT and 6.6 Re agree with spin-averaged proton fluxes (solid red circles; good estimate for the flux at 90° pitch angle) measured *in situ* by the Los Alamos Magnetospheric Plasma Analyzer instrument on the geosynchronous satellite 1994–084 at that location at 0745 UT (M. Thomsen, private communication, 2009).

4. Discussion

[11] The STEREO/STE instrument has provided the first observations of 5–26 keV ENAs from LEO and the first of ENAs from such a weak substorm (Dst > −8 nT and AE ≲ 200 nT). The morphology is similar to previous ENA images associated with large substorms and storms (DST < −50 nT) [e.g., *Pollock et al.*, 2003], with inferred equatorial proton distribution showing a spatial asymmetry with the maximum flux near midnight, likely associated with plasma injections from the magnetotail during the substorm. In addition, the STEREO/STE measurements show different morphologies at high and low energies: the observed ~5–20 keV ENA fluxes, averaged over the FOV of STE-D, are nearly constant with time, while the ~20–90 keV ENA fluxes decrease by a factor of 2. Assuming the ENA emission does not evolve during the 7-minute observation time, we found that the injected ~5–20 keV protons have a maximum at midnight with a ~145° FWHM, while the ~20–90 keV protons have a peak at 2240 MLT with a ~80° FWHM. On the night side, the MLT distribution of the ~20–90 keV protons exhibits a clear asymmetry, but we cannot rule out that the distribution of the ~5–20 keV protons may be constant with MLT. If the protons were injected from the magnetotail to $L \sim 6$ at the time of the rise of the AE index (~20 minutes before the ENA observation), then the faster gradient and curvature drift of the higher energy protons would result approximately the observed difference in local time between the 20–90 keV peak and the 5–20 keV peak. These ENA images of ring-current protons injected during a very weak substorm indicate that small substorms also contribute to the intensity and dynamics of the ring current.

[12] This study has shown that the STE type of instrument, using SSDs with very low energy thresholds and thin windows, can achieve high sensitivity, high energy resolution, and fine temporal resolution (≲1-minute, faster during large storms) for imaging of the magnetospheric ENAs, allowing detailed study of the development in space and time, while requiring about an order of magnitude less resources. A modified version of STE called STEIN (SupraThermal Electron, Ion, & and Neutral), with an electrostatic deflection system to separate ENAs from in situ electrons and low-energy ions, will be flown on the NSF-funded CINEMA (Cubesat for Ion, Neutral, Electron,

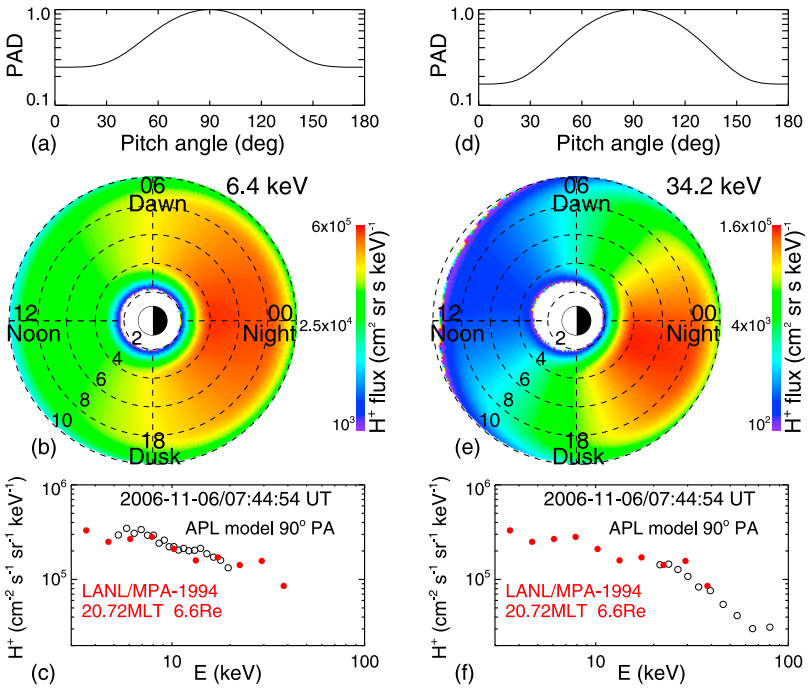

Figure 4. The normalized PAD of extracted equatorial protons of (a) 5–20 keV and (d) 20–90 keV and the spatial distribution of extracted equatorial protons at (b) 6.4 and (e) 34.2 keV. The dash-line circles indicate the L shell of 2, 4, 6, 8 and 10 in the equatorial plane. (c and f) Red solid circles show the proton fluxes measured at 2043 MLT and 6.6Re by the geosynchronous satellite 1994–084. Black open circles show the extracted proton fluxes at the same location at energies below 20 keV (c) and above 20 keV (f).

MAgnetic fields) mission planned for launch in late 2011; two more CINEMAs are planned to be developed and flown by Kyung Hee University (as part of the Korean World Class University program) to provide stereo ENA imaging and multi-point *in situ* charged particle measurements.

[13] **Acknowledgments.** We thank Marc Pulupa for help with the STEREO ephemeris, Ensang Lee for help with coordinate conversion, and Michelle Thomsen for providing the ion fluxes observed by the Los Alamos geosynchronous MPA instrument. The research at Berkeley was supported in part by NASA grant NAS5-03131 and NNX09AG33G. R. Lin was also supported in part by the WCU grant (R31-10016) funded by the Korean Ministry of Education, Science and Technology. J.P.E. holds a STFC Advanced Fellowship at ICL. E.C.R. and P.C.B. acknowledge partial support under the JHU/APL Subcontract 799106L from SwRI as a part of the TWINS NASA Explorer mission.

References

Chen, M. W., J. L. Roeder, J. F. Fennell, L. R. Lyons, and M. Schulz (1998), Simulations of ring current proton pitch angle distributions, *J. Geophys. Res.*, *103*(A1), 165–178.

C:son Brandt, P., S. Barabash, E. C. Roelof, and C. J. Chase (2001), Energetic neutral atom imaging at low altitudes from the Swedish microsatellite Astrid: Extraction of the equatorial ion distribution, *J. Geophys. Res.*, *106*, 25,731–25,744.

C:son Brandt, P., et al. (2002a), IMAGE/high-energy energetic neutral atom: Global energetic neutral atom imaging of the plasma sheet and ring current during substorms, *J. Geophys. Res.*, *107*(A12), 1454, doi:10.1029/2002JA009307.

C:son Brandt, P., Y. Ebihara, S. Barabash, and E. C. Roelof (2002b), Energetic neutral atom images of a narrow flow channel from the plasma sheet: Astrid-1 observations, *J. Geophys. Res.*, *107*(A10), 1273, doi:10.1029/2001JA000230.

DeMajistre, R., P. C. Brandt, E. C. Roelof, and D. G. Mitchell (2008), Using measurements of Energetic Neutral Atoms from low Earth orbit to infer global magnetospheric ion distributions, *J. Geophys. Res.*, *113*, A08225, doi:10.1029/2007JA012915.

Frank, L. A. (1967), On the extraterrestrial ring current during geomagnetic storms, *J. Geophys. Res.*, *72*(15), 3753–3767.

Guzik, T. G., M. Miah, J. Mitchell, and J. Wefel (1989), Low-altitude trapped protons at the geomagnetic equator, *J. Geophys. Res. 94*(A1), 145–150.

Henderson, M. G., et al. (1997), First energetic neutral atom images from Polar, *Geophys. Res. Lett.*, *24*, 1167–1170.

Hsieh, K. C., et al. (2009), A re-interpretation of STEREO/STE observations and its consequences, *Astrophys. J.*, *694*, L79–82.

Lin, R. P., et al. (2008), The STEREO IMPACT Suprathermal Electron (STE) instrument, *Space Sci. Rev.*, *136*, 241–255.

Luhmann, J. G., et al. (2008), STEREO IMPACT investigation goals, measurements, and data products overview, *Space Sci. Rev.*, *136*, 117–184.

Mitchell, D. G., K. C. Hsieh, C. C. Curtis, D. C. Hamilton, H. D. Voss, E. C. Roelof, and P. C:son-Brandt (2001), Imaging two geomagnetic storms in energetic neutral atoms, *Geophys. Res. Lett.*, *28*, 1151–1154.

Moritz, J. (1972), Energetic protons at low equatorial altitudes: A newly discovered radiation belt phenomenon and its explanation, *Z. Geophys.*, *38*(4), 701–717.

Østgaard, N., et al. (2003), Neutral hydrogen density profiles derived from geocoronal imaging, *J. Geophys. Res.*, *108*(A7), 1300, doi:10.1029/2002JA009749.

Pollock, C. J., et al. (2001), First medium energy neutral atom (MENA) images of Earth's magnetosphere during substorm and storm-time, *Geophys. Res. Lett. 28*(6), 1147–1150.

Pollock, C. J., et al. (2003), The role and contributions of Energetic Neutral Atom (ENA) imaging in magnetospheric substorm research, *Space Sci. Rev.*, *109*, 155–182.

Roelof, E. C. (1987), Energetic neutral atom image of a storm-time ring current, *Geophys. Res. Lett.*, *14*, 652–655.

Roelof, E. C., and A. J. Skinner (2000), Extraction of ion distributions from magnetospheric ENA and EUV images, *Space Sci. Rev.*, *91*, 437–459.

Roelof, E. C., D. G. Mitchell, and D. J. Williams (1985), Energetic neutral atoms (E ~50 keV) from the ring current: IMP 7/8 and ISEE 1, *J. Geophys. Res.*, *90*, 10,991–11,008.

Snyder, J. P. (1987), Map projections: A working manual, *U.S. Geol. Surv. Prof. Pap.*, *1395*, p. 182.

Vallat, C., et al. (2004), First comparisons of local ion measurements in the inner magnetosphere with energetic neutral atom magnetospheric image inversions: Cluster-CIS and IMAGE-HENA observations, *J. Geophys. Res.*, *109*, A04213, doi:10.1029/2003JA010224.

P. C. Brandt and E. C. Roelof, Johns Hopkins University Applied Physics Laboratory, 11100 Johns Hopkins Rd., Laurel, MD 20723-6099, USA.

D. W. Curtis, J. P. Eastwood, D. E. Larson, R. P. Lin, J. G. Luhmann, G. K. Parks, J. G. Sample, and L. Wang, Space Sciences Laboratory, University of California, Berkeley, CA 94720-7450, USA. (windsound@ssl.berkeley.edu)